Improving prediction of particle size with a novel acoustic bedload monitoring system consisting of phased microphone arrays and accelerometer

Zheng Chen[1], Siming He[3], Alexandre Badoux[2], Dieter Rickenmann[2]

[1]State Key Laboratory of Geohazard Prevention and Geoenvironment Protection, Chengdu University of Technology, Chengdu, 610059 China

[2]Swiss Federal Institute for Forest, Snow and Landscape Research WSL, Birmensdorf, 8903 Switzerland

[3]Institute of Mountain Hazards and Environment, Chinese Academy of Sciences, Chengdu, 610041 China

Correspondence to: Zheng Chen (zheng.chen@cdut.edu.cn, chenzcas@gmail.com)

Abstract. Accurate measurement of bedload transport flux in rivers remains an important issue in hydraulic engineering. Acoustic-based devices provide a promising way to measure the transport rate with established calibration relationships between the signal and bedload particles. We develop a novel acoustic bedload monitoring system with phased microphone arrays (PMA) and accelerometer to localize the particle impact location and to better determine the particle size. Impact experiments with quartz spheres in a flume setting were performed to investigate the dynamic signal response of the PMA monitoring system for varying particle size and impact location. For a similar virtual set-up, the conventional beamforming method was used to determine the source characteristics of the acoustic wave on the scanning plane of the PMA structure. The model provides a calculation of the cross-power matrix of the recorded pressures generated by bedload which localizes the particle impacts on the plate. The results give correlation relationships between the number of signal impulses per particle mass, the amplitude, and the centroid frequency and the bedload grain size. The findings of this study contribute to the measurement of the bedload transport with the PMA system, which helps to localize the bedload impact positions and improves the predictions of particle size.

1 Introduction

The transport of bedload in mountain rivers is responsible for the evolution of channel morphology and bedrock incision (*Turowski et al.*, 2015). Quantification of the bedload transport is needed for the study of river dynamics, for the application of hydraulic engineering structures, and for the assessment of flood hazards (*Rickenmann*, 2017). Moreover, accurate measurements of bedload transport rates help to validate empirical models that rely on experimental and field data using

traditional techniques (*Habersack and Laronne*, 2002). However, quantifying bedload transport processes particularly in steep mountain streams still remains a considerable challenge. This is mainly due to the fact that the bedload transport process is characterized by a large spatio-temporal variability (*Recking*, 2010; *Rickenmann*, 2018; *Rindler et al.*, 2023), which is

30 complicated by streambed characteristics and sediment availability.

In the past decade, considerable efforts have spurred towards the development of novel surrogate monitoring technologies, with a goal to better understand the bedload transport process especially in steep streams (*Rickenmann*, 2017; *Rickenmann et al.*, 2022). Acoustic monitoring devices, which record vibration signals generated by particle impacts, can provide continuous and accurate bedload transport data, including hydrophones (*Barton et al.*, 2010; *Camenen et al.*, 2012; *Geay et al.*, 2017;

35 *Rigby et al.*, 2016), pipe microphones (*Mizuyama et al.*, 2010), piezoelectric sensors (*Krein et al.*, 2008; *Rickenmann and McArdell*, 2007), geophones (*Rickenmann*, 2017) and seismic sensors (*Antoniazza et al.*, 2023; *Gimbert et al.*, 2019; *Roth et al.*, 2016; *Tsai et al.*, 2012). This is because the vibration signal contains useful information in the form of signal amplitude, impulse and frequency (*Barton et al.*, 2010; *Burtin et al.*, 2011; *Govi et al.*, 1993; *Hsu et al.*, 2011; *Vasile*, 2020; *Wyss et al.*, 2016a), which can be transformed to bedload transport rates and particle size classes using predefined calibration functions

40 (*Nicollier et al.*, 2021; *Wyss et al.*, 2016a; *Wyss et al.*, 2016c).

The Swiss plate geophone (SPG) system, as one of these surrogate monitoring techniques, has been deployed for bedload measurement in numerous steep mountainous streams and rivers in Europe for about 30 years (*Rickenmann*, 2017; 2023). Linear or power-law calibration functions between the electric signal and the bedload size or mass flux have been developed based on continuous data recorded by the geophone sensor, which enable for the estimation of the spatio-temporal bedload

45 fluxes in steep streams. However, considerable differences were also observed between the calibration functions obtained from the field measurement or lab-based experiments, and the linear calibration coefficients for total bedload mass flux can exhibit a variation of approximately a factor of 20 across different measurement sites (*Rickenmann and Fritschi*, 2017; *Rickenmann et al.*, 2014). This is mainly considered due to variations of impact location of bedload particles (*Turowski et al.*, 2013) and other factors, including particle shape (*Cassel et al.*, 2021; *Krein et al.*, 2008), streamflow velocity (*Wyss et al.*, 2016a), grain

50 size distribution (*Nicollier et al.*, 2021), and particle transport mode (*Chen et al.*, 2022b; *Krein et al.*, 2008; *Tsakiris et al.*, 2014). In particular, it has been found that the acoustic amplitude of the recorded signal can be decreased approximately 50% from centric to eccentric impact on the system plate (*Chen et al.*, 2022a). Considering that the spatial location of bedload particles could considerably affect the accuracy of particle size estimates using the pre-defined calibration relationships, and therefore, there is a practical need for research into a refined recognition of bedload impact locations on the plate. Furthermore,

55 well known of the impact location of bedload particle helps to improve correlation relations (electric signal vs. bedload size or mass flux) that have been developed.

To address the problem of prediction uncertainties of sediment transport arising from its spatial variations, several efforts have been made, including the use of i) dense networks of seismometers (*Antoniazza et al.*, 2023; *Bakker et al.*, 2020; *Piantini et al.*, 2022) characterized by high temporal and spatial resolution; ii) multiple characteristics of the bedload-generated signals,

60 e.g. the hybrid approach of the amplitude-frequency-based method (*Nicollier et al.*, 2022); and iii) different acoustic systems which indicate varying signal sensitivities to the bedload transport process (*Rickenmann et al.*, 2022). Given that i) the scale of investigation here is limited to the plate dimensions, and ii) the seismic waves, particularly the solid waves propagating inside the monitoring system, travel so fast (generally up to several kilometers per second in metallic materials), it is conceivable that conventional localization methods using the seismic arrival times would be very challenging within the

65 dimensions of the plate. Therefore, we consider the use of air fluctuations, which propagate at a much slower velocity than the elastic waves in solid materials, to construct a new monitoring system consisting of phased microphone arrays (PMA), which use beamforming techniques with the goal of inverting the acoustic source distribution generated by bedload impacts and localizing the spatial position of particles on the plate.

The aim of the present paper is to quantitatively investigate the effects of bedload size and particle impact location on the

70 signal response of the PMA system. The first step was to build the PMA system, which consists of a number of functional layers and acoustic sensors, including an accelerometer and an array of microphone elements. Secondly, the system was calibrated by laboratory impact experiments performed with quartz spheres of various diameters falling onto the plate at different locations. Subsequently, we used a propagation model to simulate and reconstruct an acoustic source distribution on the plate produced by the impact of a particle, which appears as an acoustic image with the center corresponding to the location

75 of the particle impact. Combined with the calibration relationship obtained from the acoustic signals, the prediction of bedload size can be eventually improved in this way.

2 Methods

2.1 Phased microphone arrays bedload monitoring system

This section presents a bedload transport monitoring system based on microphone element arrays, which consists of a number

80 of microphone sensors set at a specific spacing on the lower internal plate of the PMA system (Fig. 1). The acoustic data recorded by the microphone elements are then calculated and transformed to an acoustic source map (or so-called acoustic image), which is used to detect the position of bedload particles impacting on the plate, thereby optimizing the prediction of particle size.

The PMA system consists of a series of steel plates secured onto elastomers (elastic rubber) and embedded within a large

85 stainless steel U frame. The PMA plate is 510 mm in length, 510 mm in width and 15 mm in thickness, and has a total mass

of 30.5 kg. The elastomer layer within the PMA system serves two primary functions: (i) to reduce the transmission of vibrations to an acoustic sensor caused by bedload impacts on the surrounding material, and (ii) preventing water from entering into the system. An internal plate was pre-punched with small circular holes distributed in a matrix and bolted to the lower part of the system to hold the microphone sensors and the accelerometer (Fig. 1). The microphone element is the 4958-A

90   sensor from Brüel & Kjær, Nærum, Denmark, which is an acoustic sensor that records aerodynamic shocks of the air in the PMA system. The accelerometer currently used in this system is the 1A316E piezoelectric acceleration sensor from DHC, Jiangsu, China to record vibrations of the internal plate generated by bedload impact.
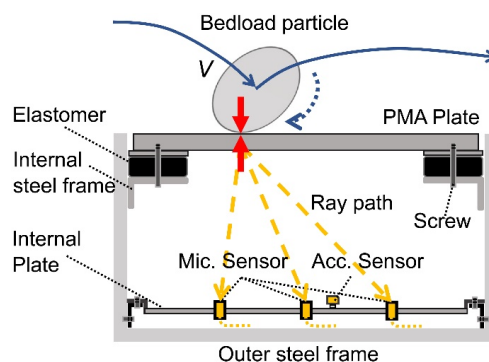
Figure 1: Sketch of a bedload particle impacting the PMA system plate at an impact velocity *V*. The yellow blocks represent the
95   **array of miniature microphone (Mic.) elements mounted on the internal plate of the PMA system. The acceleration (Acc.) sensor, which is fixed to the same plate, is also shown in yellow.**

When a bedload particle with an impact velocity *V* collides on the PMA plate, both air pressure fluctuations and structural vibrations are generated, which forces the microphone membranes and accelerometer to vibrate. A voltage potential signal (in Volts) that is proportional to the air pressure in the sensor case is induced and recorded. Also, a triggered acceleration signal

100   is measured by the accelerometer, which is related to the deformation velocity of the internal plate. The calibration coefficients of the microphone (the output voltage vs. the pressure) and the accelerometer (the output voltage vs. the acceleration) are 11.2 mV Pa^{-1} and 50.0 mV g^{-1}, respectively. The signals from both the microphones and the accelerometer are recorded at a sampling frequency of 10 kHz, using a DHC DH5902N data acquisition system with a total of 16 data channels.

2.2 Laboratory impact experiment

105   Controlled impact experiments were designed at WSL, Switzerland and were performed in the Key Laboratory of Mountain Hazards & Earth Surface Processes at IMHE, CAS in Chengdu, China to investigate the signal responses of the PMA system by controlling factors such as particle size and impact location. Systematic impact experiments were carried out with glass and quartz spheres (Fig. 2, Tab. 1) of known particle mass ranging from 9.5×10^{-3} kg to 2.2×10^{1} kg and diameter ranging from 20 mm to 116 mm. A height vernier caliper, as shown in Fig. 2a, was used to control the drop distance (the height measured from

110   the sphere center to the plate surface), i.e. 100 mm for each size class. The impact velocity of each sphere colliding onto the

PMA plate, in both water and air, was calculated using experimental image frames recorded by a high-speed camera mounted

with a side view (Fig. 2a). Different particle impact locations were designed as a 4×4 matrix, i.e. a total of 16 positions (see

Fig. 2b) from centric to eccentric on the plate. The impact tests were repeated ten times for each sphere on each impact location

in both air and water environment. The signal characteristics of the PMA system, generated by quartz spheres impacting

115   vertically onto the plate, were then analysed. The detailed information can be found in Tab. 1.
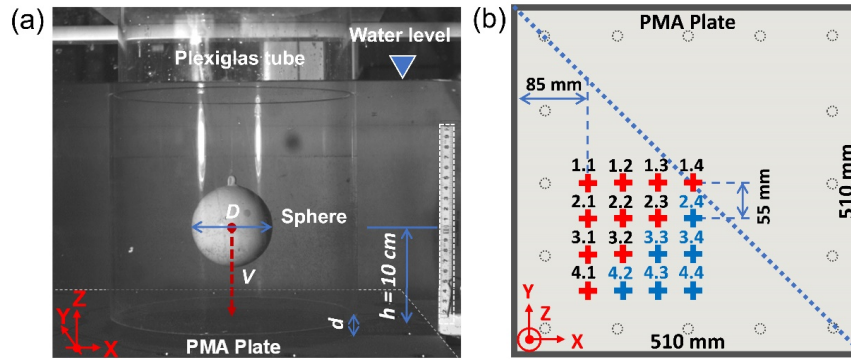
Figure 2: (a) Side view of the dropping sphere during the laboratory experiments. (b) Design of the particle impact locations "+" on the plate of the phased microphones array (PMA) bedload monitoring system. The signal data generated by particles impacting on the locations coloured in red (1.1, 1.2, …, 4.1) are used for calibration, while the data generated by particles impacting on the locations

120   **marked in blue (2.4, 3.3, …, 4.4) are for validation.**

Table 1: Characteristic values, including particle diameter D, mass M, particle density ρ_s, and impact velocity V (V_A and V_W) of the spheres hitting at 16 impact positions (from 1.1 to 4.4) on the plate. V_A and V_W indicate the impact velocities measured in the air and water, respectively.

Class	Material	D (m)	M (kg)	ρ_s (kg m^{-3})	V_A (m s^{-1})	V_W (m s^{-1})	Impact locations
1	Glass	0.020	0.0095	2303	1.35±0.01	1.02±0.01	1.1 to 4.4
2	Glass	0.025	0.0206	2582	1.31±0.01	1.05±0.02	1.1 to 4.4
3	Glass	0.030	0.0341	2463	1.30±0.01	1.01±0.01	1.1 to 4.4
4	Quartz	0.049	0.1706	2753	1.22±0.02	0.96±0.02	1.1 to 4.4
5	Quartz	0.079	0.7040	2765	1.11±0.03	0.88±0.04	1.1 to 4.4
6	Quartz	0.100	1.4386	2748	1.02±0.04	0.80±0.04	1.4, 2.3, 3.2, 4.1
7	Quartz	0.116	2.2420	2715	1.00±0.04	0.72±0.05	1.4, 2.3, 3.2, 4.1

2.3 Conventional beamforming technique

125   The basic principles of the conventional beamforming technique are described in this section, with the first step being to

calculate the Fourier transforms of the recording pressure data for each microphone element of the array, as shown in **Eq. 1**.

$$\mathbf{p} = [p_1(f), \dots, p_N(f)]^{\mathrm{T}} , \tag{1}$$

where $p_i(f)$ $(i = 1, \dots, N)$ are the components of the N-dimensional vector $\mathbf{p}$ that are obtained by fast Fourier transform (FFT) on the recorded signals, N is the number of microphone sensors, $[\cdots]^{\mathrm{T}}$ represents the transpose of the vector.

130 A propagation model to calculate the acoustic signal at the microphone locations can be selected as the "steering vector" $\mathbf{g}$ (see **Eq. 2**), considering each node of scanning plane as a hypothetical sound source (see Fig. 3). The components $g_{j,m}$ of $\mathbf{g}$ indicate the amplitude of the pressure signals recorded by the microphone sensors induced by an ideal sound source with unit strength.

$$g_{j,m} = \frac{1}{4\pi \|x_m - \xi_j\|} e^{-2\pi i f \Delta t_{j,m}} , \tag{2}$$

135 where x_m is the coordinate vector of microphone sensor m, ξ_j is the coordinate vector of node j on the scanning plane, $i^2 = -1$, and $\Delta t_{j,m}$ is the emission time delay that can be expressed as:

$$\Delta t_{j,m} = \frac{\|x_m - \xi_j\|}{c} , \tag{3}$$

where c is the speed of sound.

Since **Eq. 2** indicates the pressure amplitude induced by the unit-strength sound source, the complex amplitude A_s of the

140 sound source must now be determined. One consideration is to minimize the following comparison (*Sijtsma*, 2010), which indicates the differences D_{pg} between the measured or recorded pressure vector $\mathbf{p}$ and the calculated pressure vector $A_s\mathbf{g}$.

$$D_{pg} = \|\mathbf{p} - A_s\mathbf{g}\|^2 , \tag{4}$$

Eq. 4 can be fully rewritten as:

$$D_{pg} = \|\mathbf{g}\|^2 A_s^2 - 2\mathbf{g}^*\mathbf{p} A_s + \|\mathbf{p}\|^2 , \tag{5}$$

145 The minimization solution of **Eq. 5** is given as $\frac{1}{4\|\mathbf{g}\|^2}(4\|\mathbf{g}\|^2\|\mathbf{p}\|^2 - \|2\mathbf{g}^*\mathbf{p}\|^2) = 0$ when

$$A_s = \frac{\mathbf{g}^*\mathbf{p}}{\|\mathbf{g}\|^2} , \tag{6}$$

In general, it is convenient to consider the source auto-powers in the case of broadband noise as:

$$A_{sa} = \frac{1}{2} A_s A_s^* = \frac{1}{2} \frac{\mathbf{g}^*\mathbf{pp}^*\mathbf{g}}{\|\mathbf{g}\|^4} , \tag{7}$$

If the $N \times N$ cross-power matrix of the measured pressures is defined as $\mathbf{C}$:

150 $$\mathbf{C} = \frac{1}{2}\mathbf{pp}^* , \tag{8}$$

where $\mathbf{p}^*$ is the complex conjugate transpose of $\mathbf{p}$, then the calculated amplitude of the sound source can be written as:

$$A_{sa} = \mathbf{w}^* \mathbf{C} \mathbf{w} \, , \tag{9}$$

where $\mathbf{w}$ is the weighted steering vector and can be expressed as:

$$\mathbf{w} = \frac{\mathbf{g}}{\|\mathbf{g}\|^2} \, , \tag{10}$$

155   With the above cross-power matrix $\mathbf{C}$ (**Eq. 8**) and the weighted steering vector $\mathbf{w}$ (**Eq. 10**), the strength of acoustic pressure

over the nodes of the scanning plane can be calculated, resulting in an image of the sound source.
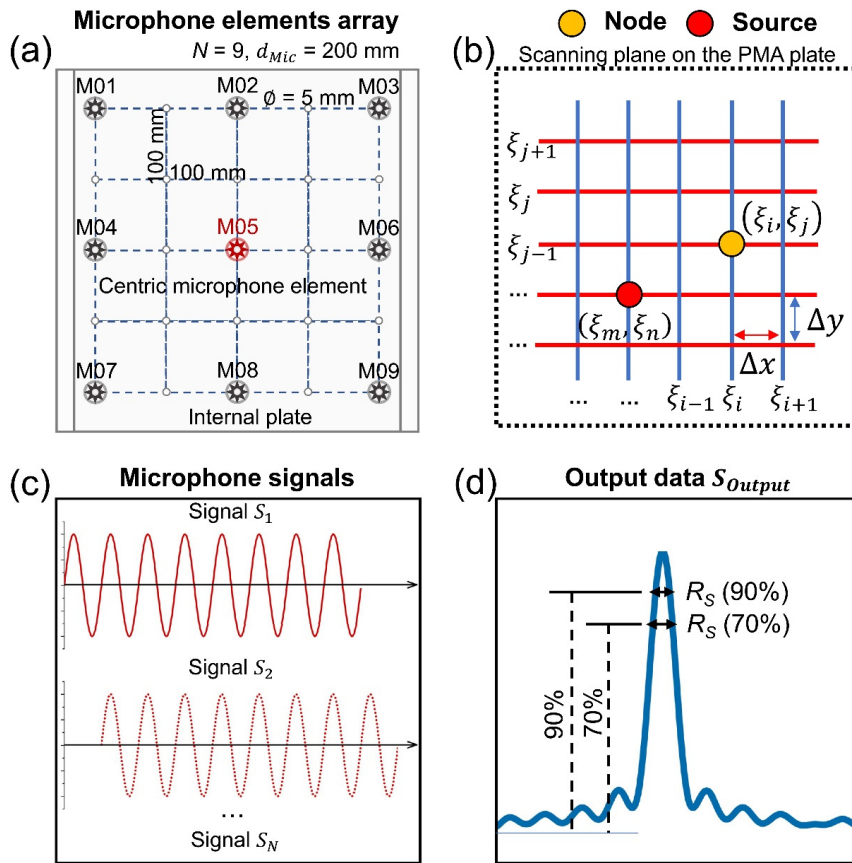
Figure 3: Numerical model for the analysis of acoustic source generated by bedload particle impacts. (a) Sketch of the microphone
elements mounted on the internal plate of the PMA system at a spacing distance of $d_{Mic} = 200$ mm, where the element in the centric
160   **position of the internal plate is marked in red. (b) Scanning plane with a standard rectangular grid and surface dimensions of**
$L_{PMA} \times W_{PMA}$ m², where L_{PMA} and W_{PMA} are the length and width of the PMA plate, respectively. (ξ_i, ξ_j) indicates a node of the
scanning plane on the plate, while (ξ_m, ξ_n) is the source location on the PMA plate. Illustration of (c) input and (d) output signal
data during the numerical procedure.

2.4 Numerical simulation

165   In this section, numerical examples are presented to show the results of the reconstruction of the impact-induced acoustic

source for a single bedload particle (monopole source) and for multiple particles (multipole sources) at different impact locations and spacing distances. In addition, the effects of the arrangement of the microphone elements and the frequency of the source emission signal on the reconstructed acoustic image are estimated using numerical methods.

2.4.1 Numerical simulation procedure

170 Due to the fact that the real sound source is distributed in three dimensions, a reconstruction of sound source necessitates numerical scanning and calculation based on 3D grids and nodes, resulting in a rather long computation time for 3D source localization. However, given that the approximately parallel spatial relationship between the PMA plate surface and the riverbed, and we only focus on impact positions of bedload particles on the plate or bed. Therefore, the three-dimensional grid collapses to a two-dimensional grid plane, which greatly simplifies the numerical calculations.

175 Numerical simulations are conducted with a planar array of N microphone elements positioned on the internal plate (in the plane Z = 0 m) of the PMA system, as illustrated in Fig. 3. A monopole source (Mon.) and multipole sources (Mul.) are simulated above the microphones array, respectively, which are located on the surface plate (in the plane Z = 0.25 m) of the PMA system. Subsequently, an acoustic scan is carried out on the scanning plane (Z = 0.25 m) with a surface of $L_{PMA} \times W_{PMA}$ m², using a standard rectangular grid with a size of 0.01 m. The scanning plane during numerical procedure covers the PMA

180 plate dimensions in length L_{PMA} and width W_{PMA}, ranging from 0 m to 0.51 m, which totally contains $N_{Grid} = 1.02 \times 10^4$ grid points using the following Eq. (11). The numerical solutions of the acoustic amplitude are obtained by conducting a computational procedure in both X and Y directions, assuming that each node of the grid is an acoustic source. Consequently, the result of this scanning process over the entire grid is presented as the acoustic image, as seen in the following section.

$$N_{Grid} = \left(\frac{L_{PMA}}{\Delta x} + 1\right)\left(\frac{W_{PMA}}{\Delta y} + 1\right) , \tag{11}$$

185 where Δx and Δy are grid sizes in the X and Y directions.

2.4.2 Microphone elements arrangement

Figure 3a displays an array with $N = 9$ microphone elements, where the number of elements and the spacing, d_{Mic}, are mutually constrained because the structural dimensions of the PMA system have been predetermined. Hence, the planar dimensions of the PMA in terms of its length L_{PMA} and width W_{PMA} control the distribution range of the microphone element arrays, while

190 the height H_{PMA} constraints the wave propagation distance from the sound source to the element arrays.

An illustration of the output source plot from the scanning process over the grids (Fig. 3b) using the microphone signals (Fig. 3c) is presented in Fig. 3d which is also called "beam pattern" and generally ranges in dB. The beam pattern consists of the main lobe which is determined by the peak value and its neighbourhood and a number of side lobes. The resolution R_S of the

array can be then defined as the value of the beamwidth (width of the main lobe) that covers a range of 3 dB in general or 30%

and 10% below the peak value for the present study, as shown in Fig. 3d. The beamwidth shows dependencies on signal

frequency, wave propagation distance, microphone arrangement, beamforming algorithm, etc. In particular, the spacing of the

array element d_{Mic} is an important parameter controlling the characteristics of beam pattern of the reconstructed acoustic source,

especially the beamwidth.

Theoretical and computational calculations show that the beamwidth decreases with increasing array spacing d_{Mic} and the

signal frequency. Generally, in array and beamforming design we want a sharper beam (relatively higher main lobe and lower

side lobes), which indicates more concentrated energy in the beam pattern. Hence, the value of d_{Mic} can be adjusted

appropriately to achieve optimal results. However, a large value of d_{Mic} can produce undesirable outcomes, such as noise

suppression. In particular, spatial aliasing occurs when d_{Mic} is larger than the half-wavelength of signal, resulting in less

differentiation between the main and side lobes. Therefore, on the internal plate of the PMA system, the designed value of

array spacing d_{Mic} must satisfy the Nyquist sampling theorem, that is,

$$d_{Mic} \leq \frac{1}{2}\lambda \ , \tag{12}$$

where $\lambda = c/f$ is the wavelength of signal; c is the speed of sound, 340 m s^{-1}; f is the characteristic frequency of the signal.

During the numerical simulations, given that $f = 1600$ Hz, then $d_{Mic} \leq 106.3$ mm, and the angular frequency w and wave number

k are calculated to be 10048 Hz and 29.6 m^{-1}, respectively, as shown in Tab. 2.

2.4.3 Numerical tests

The principle is to use a number of microphone elements (as few as possible) equipped on the internal plate to localize the

spatial position of the bedload particles. During the numerical tests, we firstly calculate the received signals for each

microphone element from an emission signal (a periodic cosine signal is considered here), by using the propagation model

(steering vector **g**). Next, a white noise is added to the received signal of each microphone element, with the signal-to-noise

ratio (SNR) of 10. Consequently, an acoustic image of the sound source can be reconstructed through the beamforming

technology. Some relevant parameters which are used in the numerical simulations can be seen in Tab. 2. In the numerical

simulations, $N = 3$ to 25 microphone elements are used, with varied layouts (see descriptions in Appendix A).

Table 2: Characteristic parameters of the sound source used for numerical simulations, including sound speed c, sampling frequency f_S, block length T, frequency of interest f, angular frequency w, wave number k, number of microphone elements N, signal-noise ratio SNR, grid size in the X and Y directions, Δx and Δy respectively.

Parameter	Description	Value	Unit
c	speed of sound	340	m s^{-1}
f_S	sampling frequency	10000	Hz

T	block length	0.1	s
f	frequency of interest	1600	Hz
w	angular frequency $w = 2\pi f$	10048	Hz
k	wave number $k = w\,c^{-1}$	29.6	m^{-1}
N	number of microphone elements	3-25	-
SNR	signal-noise ratio	10	-
Δx	grid size in the X direction	0.01-0.03	m
Δy	grid size in the Y direction	0.01-0.03	m

2.5 Experimental signal processing

2.5.1 Maximum amplitude

Acoustic signals, including microphone signals and acceleration vibrations, can be triggered by bedload impacts and recorded by the PMA system. Typical signals recorded by the centric microphone element (M05 mounted at the centric position of the

225   internal plate of the PMA system, Fig. 3a) during an impact experiment for a 24.8 mm diameter quartz sphere impacting the PMA plate at the centric location 1.4 are shown in Fig. 4a. A packet is defined as an envelope (see blue lines in Fig. 4) of the raw signals which is computed with Hilbert transform as introduced by *Wyss et al*., (2016a), reflecting an impact event of a particle hitting on the plate. The packet-based amplitude histogram method was developed by *Wyss et al*. (2016a) to derive bedload size information from geophone data recorded by the SPG system, through a predefined calibrated power-law

230   relationship.

$$A_{Pac,j} = \alpha D_j^{\beta} \ , \tag{13}$$

where $A_{Pac,j}$ indicates the mean amplitude (V) of a signal packet for each class j, D_j (mm) is the mean particle size for class j, and the two coefficients α and β in Eq. (13) are determined by calibrated laboratory experiments or field bedload measurements.

235   In the present study, we follow the above method to determine a packet of acoustic signals generated by a falling sphere impacting on the PMA plate. Based on the calculated packet, the positive maximum amplitude of the generated signal is defined as $A_{Max,P}$ in voltage (V) and the packet length (time duration) is determined as L_P, as shown in Fig. 4a. In addition to studying the signal characteristics within an entire envelope, we also focus on the effective "first wave" of the signals, as its physical properties are more significant than the entire signals following reflections, as illustrated in Figs 4d and 4e. The length

240   of the effective first wave is approximately one to two milliseconds, whereas L_P typically lasts tens to hundreds of milliseconds.

2.5.2 Signal impulses
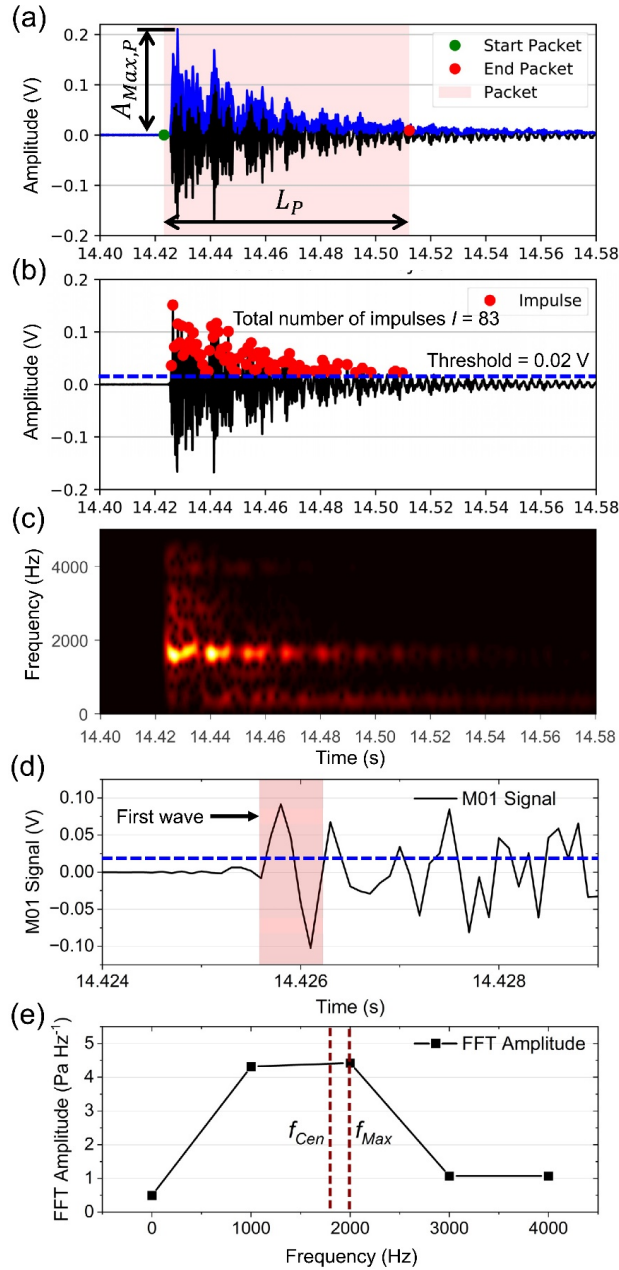
Figure 4: Illustration of the internal plate vibrations of the PMA system generated by a centric impact with a sphere of 24.8 mm in diameter. (a) The signals in the vertical direction were generated by a centric impact (location 1.4) onto the PMA plate with a velocity

245 **of 1.05 m s⁻¹. A signal packet (see solid blue line) was presented as an envelope of the signal, which was computed with the Hilbert transform. (b) Signal impulses I = 83 were counted as the number of times the signal exceeded the threshold value (see dashed horizontal blue line) that is defined as 0.02 V in the positive domain. (c) Spectrogram of the vibration signals. (d) Illustration of the first wave. (e) The calculation of the centric f_{Cen} and peak f_{Max} frequency of the first wave signal.**

A packet contains a number of impulses I which can be obtained by counting the number of times the positive signal peaks

250   cross the pre-defined amplitude threshold (*Rickenmann et al.*, 2014; *Wyss et al.*, 2016b), as illustrated in Fig. 4. On the basis

of impulses counting, we further define a calibration coefficient. This is the number of impulses per particle mass k_{IPM} (see

Eq. (14)), which indicates the signal vibrations triggered by a single particle impact.

$$k_{IPM_{i,j}} = \frac{I_{i,j}}{M_{i,j}} \,,$$ (14)

where $I_{i,j}$ are the signal impulses recorded by the system and generated by a single particle impact for an experimental run *i*

255   and particle size class *j*, and $M_{i,j}$ is the corresponding mass of that particle.

2.5.3 Centroid frequency

The centric frequency f_{Cen} of the plate vibrations is proposed as an important parameter which helps to identify the bedload

particle size, according to the Hertz contact theory (*Chen et al.*, 2022a; *Johnson*, 1985; *Rickenmann*, 2017; *Thorne*, 1986 and

2014). In this study, the frequency spectrum of a signal packet is determined by a fast Fourier transform (FFT), and the centric

260   frequency of the microphone and acceleration signal of a packet are computed as $f_{Cen,Mic}$ and $f_{Cen,Acc}$, respectively, using

the following Eq. (15). With regard to the signal of the first wave, we also consider calculating its centric frequency as well as

peak frequency f_{Max}, as seen in Fig. 4e.

$$f_{Cen} = \frac{\sum f_m A_{FFT,m}}{\sum A_{FFT,m}} \,,$$ (15)

where f_m is the spectrum frequency (Hz) and $A_{FFT,m}$ is the amplitude (V·Hz⁻¹) which is calculated by performing FFT on

265   the recorded signals.

3 Results

3.1 Performance of microphone elements array

3.1.1 Number of microphone elements
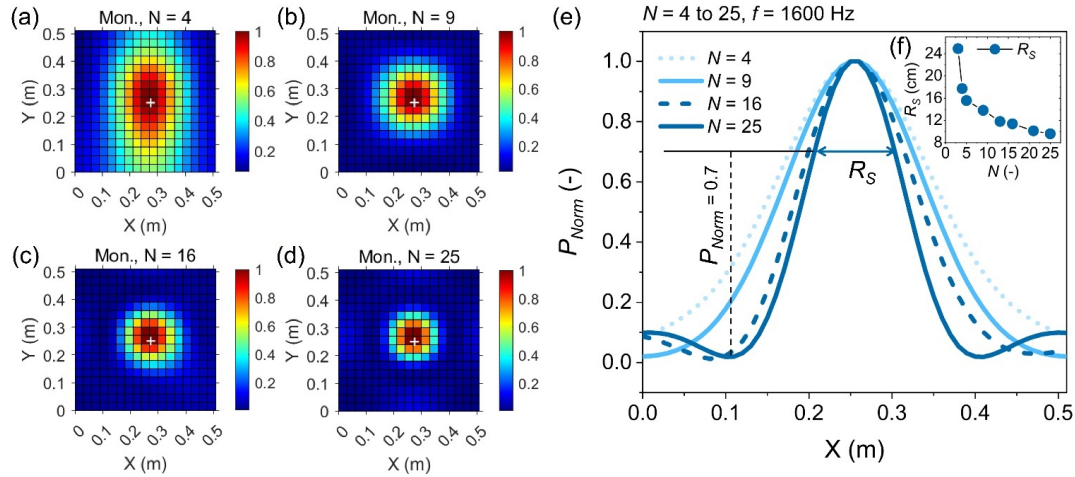
Figure 5: The acoustic image and beam pattern determined with varied microphone element numbers *N* ranging from 3 to 25. (a), (b), (c), and (d) The acoustic images derived from the monopole source (Mon.) at the centric location of the PMA plate, obtained by using the beamforming technology with different numbers of microphones *N* = 4, 9, 16, 25, respectively. The colour bar indicates the non-dimensional acoustic intensity P_{Norm}, representing the value of the reconstructed acoustic pressure normalized by the maximum amplitude at the center of the acoustic image. (e) The corresponding beam patterns of *N*-sensor arrays when d_{Mic} = 100 mm and frequency *f* = 1600 Hz for monopole sources. (f) Resolution of the beam pattern as a function of *N* (ranging from 3 to 25). The emission coordinate (0.255, 0.255) is at the center of the plane, as marked by the white cross "+".

Figure 5 shows the acoustic images of monopole sources (Mon.) determined with a number of microphone elements *N*. The results of pressure distribution are displayed and normalized by the maximum amplitude of the main lobe. Figures 5a to 5d present the monopole source images determined with *N* = 4, 9, 16, 25, respectively. Figure 5e plots the corresponding beam patterns, with d_{Mic} = 100 mm, and *f* = 1600 Hz, for different microphone arrays. The beam pattern consists of a total of one main lobe for *N* = 4 and 9, while two side lobes appear for *N* = 16 and 25. According to the results, the resolution value of the beam pattern becomes finer as the number of microphone sensors increases, with *N* ranging from 3 to 25, as seen in Fig. 5f.

3.1.2 Microphone elements arrangement
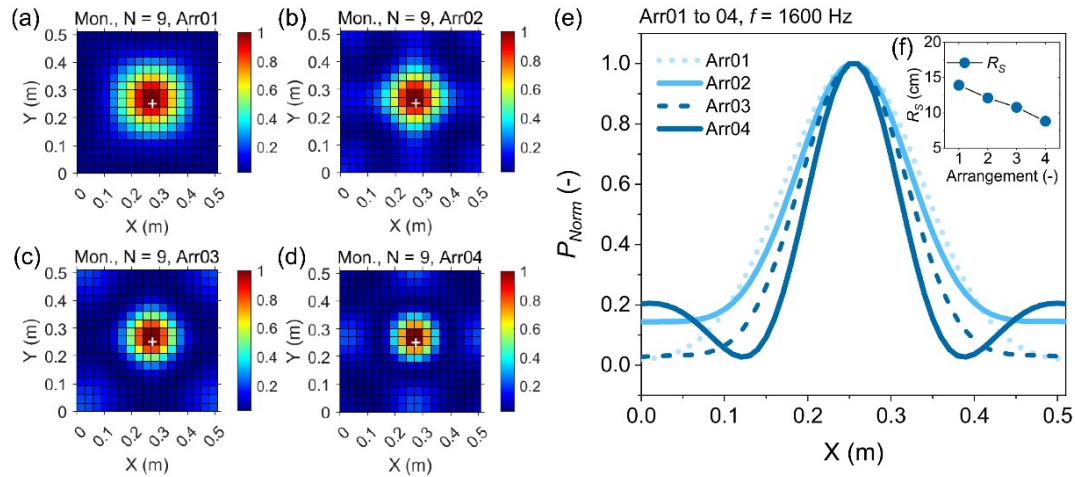
Figure 6: The acoustic image and beam pattern determined with different microphone element arrangements. (a) to (d) The acoustic images for a monopole source determined with microphone element arrangements Arr01 to Arr04, respectively. (e) The beam patterns of the 9-sensor array for different element arrangements Arr01 to Arr04, with d_{Mic} = 100 mm and f = 1600 Hz for monopole sources, respectively. (f) Resolution of the beam pattern for Arr01 to Arr04. See the caption of Fig. 5 for details regarding the colour scale.

The acoustic images shown in Figs 6a-6d are determined with nine microphone elements for the four different sensor arrangements Arr01-Arr04. Figure 6e plots the corresponding beam patterns with N = 9, d_{Mic} = 100-200 mm, and f = 1600 Hz, for different microphone arrangements. The spacing distances d_{Mic} between microphone elements in an array range from 100 mm to 200 mm when changing their arrangement from Arr01 to Arr04, see Appendix A more information. The results indicate that the microphone element array with the Arr04 arrangement (d_{Mic} = 200 mm) has the finest resolution of the beam pattern with the highest side lobes.

3.1.3 Locations and spacing distances of sound sources
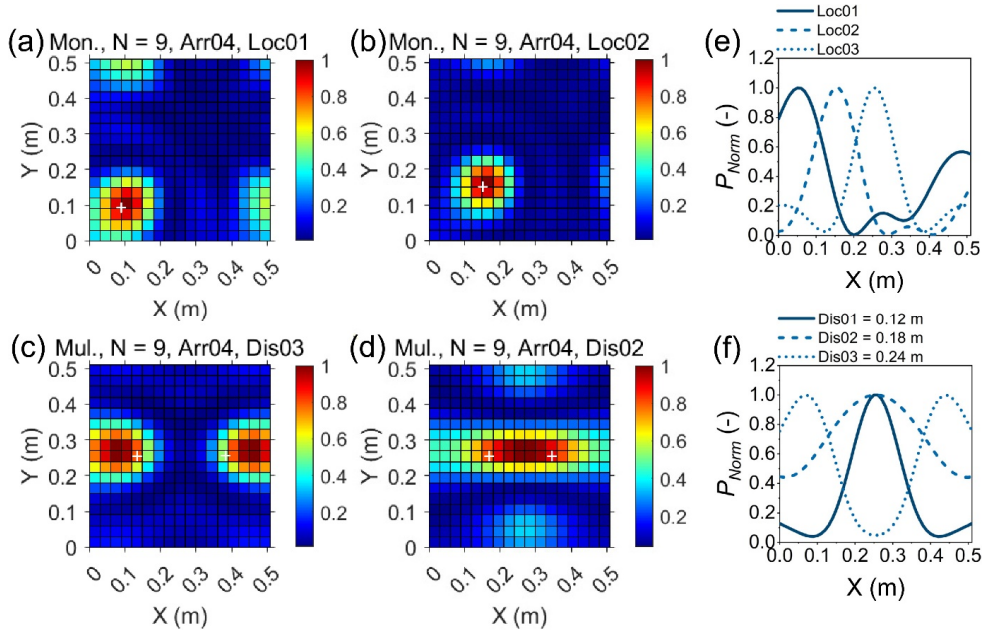
Figure 7: The acoustic image and beam pattern. The acoustic image for a monopole source with different impact locations ((a) and (b)) and for multipole sources with varying spacing distances ((c) and (d)), which are obtained by using the beamforming technology.

300 **(e) and (f) The beam patterns of the 9-sensor array when d_{Mic} = 100 mm and frequency f = 1600 Hz for monopole and multipole sources, respectively. The signal emission coordinates for (a) and (b) are (0.09, 0.09) and (0.145, 0.145), respectively. The emission coordinates for (c) are (0.135, 0.255) and (0.375, 0.255), while for (d) they are (0.165, 0.255) and (0.345, 0.255). See the caption of Fig. 5 for details regarding the colour scale.**

Figure 7 shows the reconstructed acoustic images of the sources generated with varying signal emission locations for monopole

305 sources and with different spacing distances for multipole sources (Mul.). The results of pressure distribution are displayed

and normalized by the maximum amplitude of the main lobe. Figures 7a-7b present the monopole source images under the

condition of the emission coordinates (0.09, 0.09) and (0.145, 0.145), respectively. The reconstructed acoustic images shown

in Figs 7c and 7d, on the other hand, are for multipole sources, with source spacings of 0.24 m and 0.18 m, respectively.

According to the results, the coordinates of the reconstructed acoustic source, corresponding to the center of the red-black area,

310 generally agree well with the locations of the emission signals.

Figure 7e plots the beam pattern for a microphone array with nine sensors, d_{Mic} = 100 mm, and f = 1600 Hz, for different

signal emission locations. The beam pattern consists of a total of three beams for the signal emission locations close to the

boundary of the plate. The one with the maximum amplitude is the so-called main lobe and the rest are side lobes with relatively

smaller amplitudes, as mentioned above. In contrast, the shape of the beam pattern changes, becoming more symmetrical as

315 the emission location is moved from the boundary to the plate center (0.255, 0.255). The simulation results also show that the

heights of the two side lobes decrease significantly, indicating that the grain of the noises become weaker as the location of

the emission signal approaches to center of the plate from the edge.

We also plot the beam pattern for the microphone element arrays, as above, with nine sensors for multipole sources varying in spacing distances. There are two main lobes of approximately the same amplitude, corresponding to two acoustic sources, as

320   shown in Fig. 7f. The number of beams decreases to one when the spacing is reduced. In the meantime, we see that the side lobe between the two main lobes disappears, while the amplitudes of the rest side lobes increase significantly, which indicates that the gain pattern of the competing sources becomes larger when the two sources are close to each other. Furthermore, as the spacing distance drops to 0.12 m, the number of beams in the beam pattern remains as a single beam with a much higher resolution of the main lobe. This demonstrates that the multipole sources cannot be distinguished at this point, indicating that

325   the spatial resolution for the multipole sources of the system is approximately 0.12 m under these conditions.

3.2 Signal responses of the PMA system generated by particle impacts

3.2.1 Maximum amplitude
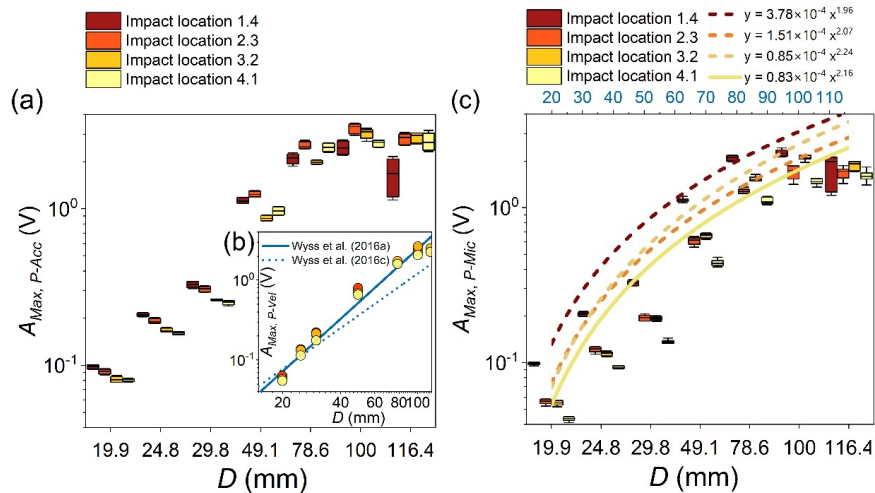
Figure 8: The maximum amplitude $A_{Max,P}$ as a function of the sphere diameter D for centric (1.4) and eccentric (2.3, 3.2, and 4.1)

330   **impacts. (a) The maximum amplitude $A_{Max,P-Acc}$ of a packet recorded by the accelerometer in the Z (vertical) direction of the PMA system. In (b), the empirical relationship based on the laboratory flume experiments of *Wyss et al.* (2016a) and the results of the field experiments at the Erlenbach site with the SPG system (*Wyss et al.*, 2016c) are presented for comparison with the $A_{Max,P-Vel}$. $A_{Max,P-Vel}$ indicates the maximum packet amplitude in voltage transformed from the velocity signals that are integrated from the accelerations in the Z direction, using the calibration coefficient of the geophone of the SPG system. The different colours of the dots**

335   **from red to yellow represent four different impact locations (1.4, 2.3, 3.2, and 4.1). (c) The maximum amplitude $A_{Max,P-Mic}$ from the microphone sensor M05 mounted at the centric position of the internal plate. Figure (c) also shows fitted lines of the maximum amplitude for different impact locations as functions of particle size class.**

To assess the signal response of the PMA system to bedload particle impacts at various spatial locations on the plate, a total of 880 bedload impacts were analyzed for particle sizes D ranging from 19.9 mm to 116.4 mm and for eccentricity distances

340   d_e ranging from 0 mm to 233.4 mm. The eccentricity distance d_e indicates the distance between the plate center of the PMA

system and the particle impact location. During the drop experiments, each impact generates 12 channels of acoustic signal data. The maximum amplitude $A_{Max,P-Acc}$ of a packet recorded by the accelerometer of the PMA system increases with increasing particle size D for both the centric (at location 1.4) and eccentric (at locations 2.3, 3.2, and 4.1) impacts, as shown in Fig. 8a. To make a direct comparison with the SPG system, we performed an additional calculation by integrating the

345   acceleration signals to obtain the deformation velocity which can be then transformed into a voltage signal using the calibration coefficient (27.6 V m^{-1} s) of the SPG geophone, as shown in Fig. 8b. An increasing trend can be observed for the $A_{Max,P-Mic}$ data recorded by the microphone element M05 (Fig. 8c). All measurements show a generally larger amplitude triggered by centric impacts compared to that induced by eccentric impacts, except for the largest particles with $D = 116.4$ mm. The differences between the centric and eccentric impacts also show an increasing trend with increasing particle size (up to size

350   class 6).

The mean of the maximum packet amplitudes $\overline{A_{Max,P}}$ for each impact location (marked in red in Fig. 2b) were obtained though repeated drop experiments across all particle size classes. Subsequently, the power-law functions were determined from the acceleration and microphone signals, respectively, as: $\overline{A_{Max,P}} = \alpha D^{\beta}$, where the coefficients α and β and the correlation coefficient R are presented in Tab. 3. Significant deviations in the signal packet amplitude induced by the largest

355   particle size class ($D = 116.4$ mm) were observed in Fig. 8, which is likely due to the small accelerating distance measured from the sphere center to the plate which is 10 cm for all size classes. Therefore, these data were not utilized for calibration.

Table 3: The coefficients in the power functions determined between the maximum amplitudes of the acceleration and microphone signals with particle size. The fitting utilized signal data generated by particle impacts at various positions on the PMA plate, with the eccentricity distance d_e ranging from 0 mm to 233.4 mm. The coefficients α_{Acc} and β_{Acc} presented in Tab. 3 indicate the
360   **values obtained from the vertical acceleration signals, while the coefficients with the subscript "Mic" were computed from the microphone (sensor M05) signals.**

Impact locations	d_e (mm)	α_{Acc} ($\times 10^{-4}$)	β_{Acc}	R	α_{Mic} ($\times 10^{-4}$)	β_{Mic}	R
1.4	0.00	3.47	1.98	0.93	3.78	1.96	0.90
1.3	55.00	1.32	2.22	0.96	1.39	2.12	0.97
2.3	77.78	1.48	2.23	0.96	1.51	2.07	0.97
1.2	110.00	1.41	2.21	0.97	1.02	2.16	0.97
2.2	122.98	0.72	2.56	0.99	0.59	2.33	0.99
3.2	155.56	1.36	2.20	0.99	0.85	2.24	0.98
1.1	165.00	1.77	2.15	0.96	0.58	2.31	0.96
2.1	173.93	1.01	2.35	0.98	0.32	2.51	0.99
3.1	198.31	0.67	2.45	0.99	0.44	2.37	0.99
4.1	233.35	1.24	2.23	0.90	0.83	2.16	0.98

3.2.2 Signal impulses
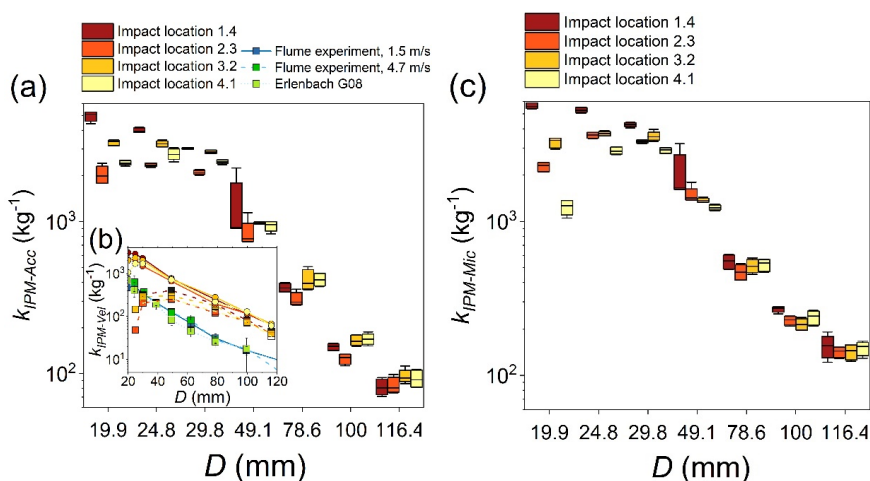
Figure 9: Relationship between the signal impulses per particle mass k_{IMP} and the quartz sphere diameter D with variable impact
365   **locations 1.4, 2.3, 3.2 and 4.1 on the PMA plate. (a) The value of $k_{IMP-Acc}$ calculated from acceleration vibrations (in the vertical**
direction). In (b), the data obtained from the flume experiments by *Wyss et al.* (2016a) for two water flow velocities (1.5 m s^{-1} and 4.7
m s^{-1}) and the results of the Erlenbach snowmelt experiments for the geophone sensor G08 are presented for comparison with the
$k_{IMP-Vel}$ values that are calculated from the integrated velocity signals. The round and square dots in (b) indicate the $k_{IMP-Vel}$ values
calculated using a threshold value of 0.02 V and 0.1 V, respectively. The different colours from red to yellow represent four different
370   **impact locations (1.4, 2.3, 3.2, and 4.1). (c) The value of $k_{IMP-Mic}$ calculated from microphone signals (recorded by the microphone**
element M05).

The drop experiments data indicate that the signal impulses per particle mass k_{IMP} depend on particle size and impact location,

with a nonlinear decreasing trend with increasing sphere size D (Fig. 9). In general, the decreasing trend of the coefficients

k_{IMP} calculated from the signals recorded by the PMA system is consistent with that determined from the flume experiments

375   by *Wyss et al.* (2016a) and the Erlenbach field site (*Wyss et al.*, 2016b) using the SPG system. However, the k_{IMP} values in our

study are within an order of magnitude larger than the data in *Wyss et al.* (2016a and 2016b), except for the two smallest

particle size classes when using a threshold value of 0.1 V (Fig. 9b). Also, the influence of the particle impact location on the

impulse-mass coefficient k_{IMP} is greater for the smallest serval classes than for the remaining size classes.

3.2.3 Centroid frequency
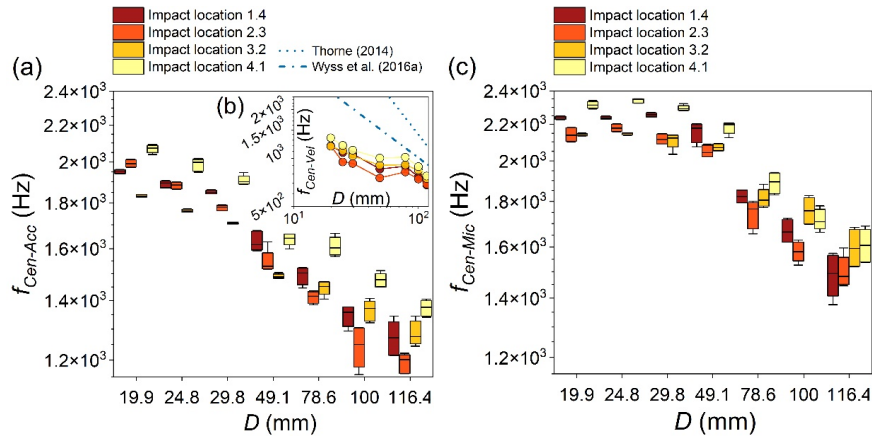
380

Figure 10: Relationship between the centroid frequency f_{Cen} of the generated signals and the quartz sphere diameter D for variable impact locations. The centroid frequency was calculated from (a) acceleration vibrations (in the vertical direction) (b) velocity signals integrated from the vertical accelerations, and (c) microphone signals (recorded by the microphone sensor M05). Figures (a) to (c) display the data generated by particles impacting the plate at the locations 1.4, 2.3, 3.2 and 4.1 indicated by colours from red to

385 **yellow.**

From the drop experiments, the centroid frequencies $f_{Cen-Acc}$, $f_{Cen-Vel}$ and $f_{Cen-Mic}$ of the signals of acceleration, integrated velocity, and microphone sensors, respectively, generally decrease with increasing sphere size D for all impact locations (Fig. 10). For the different sphere classes, the value of f_{Cen} for the eccentric impact at the location 4.1 is generally the largest. For particle size D ranging from about 78.6 mm to 116.4 mm, the $f_{Cen-Acc}$ values are in fairly good agreement with the contact model

390 (*Thorne*, 2014). However, for the smallest size classes, our data show better agreement with the flume experiment results (*Wyss et al.*, 2016a). The empirical model proposed by *Wyss et al.* (2016a) is approximately 2.0 and 1.3 times as large as the value of $f_{Cen-Vel}$ for the smallest four particle size classes and the largest three size classes ranging from 78.6 mm to 116.4 mm. In general, the values of $f_{Cen-Mic}$ are larger than those of $f_{Cen-Acc}$.

3.3 Acoustic source image reconstructed using the PMA data

395 Acoustic images of the source calculated from the measured signals of the PMA system are presented in overhead view in Fig. 11. They show the intensity of the air shock on the underside of the PMA plate after centric and eccentric impacts of a class 4 sphere ($D = 49$ mm). The impact location of the sphere is indicated by the center of the main lobe in the reconstructed acoustic image. The acoustic intensity is normalized by the maximum amplitude at the center of the acoustic image.

Figures 11a and 11b display the acoustic images obtained with the centroid frequency and the peak frequency, respectively, as

400 the frequency of interest in the calculation process, using the signals within the entire packet generated by a particle impact at the center of the plate and recorded by the array of microphone elements. For comparison, Fig. 11c shows the results calculated

using only the first wave signal from the microphone array. The comparison between Figs 11a, 11b and 11c reveals that the

use of signals induced by the entire impact event leads to very complex results, mainly showing an increase of the side lobes,

which is a challenge for the derivation of particle location information. In contrast, calculations using only the first wave

405   information from the microphone array produced generally good results. We also present the acoustic images obtained using

the experimental signals for eccentric impacts (e.g. Loc2.3, Loc 3.2 and Loc4.1; Figs 11d-11f) to facilitate comparison between

results from different impact locations.
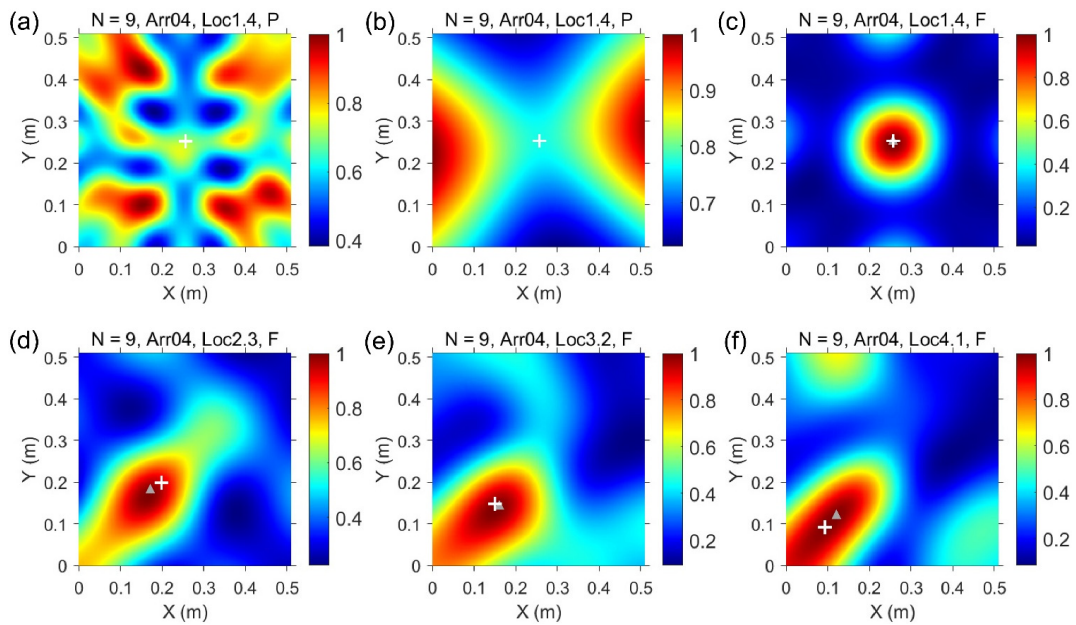
Figure 11: The acoustic image of a monopole source triggered by eccentric and centric impacts. (a) and (b) The results obtained with
410   **the centroid (a) or peak (b) frequency as the frequency of interest in the calculation process, using the signals within the entire packet**
"P" generated by a particle impact at the center of the plate "Loc1.4", marked by the white cross "+". (c) The results which are
calculated using only the signal of the first wave "F" from the microphone array. (d), (e) and (f) The acoustic images are determined
using experimental signals (the first wave) for eccentric impacts, e.g. Loc2.3, Loc 3.2, and Loc4.1, respectively. The triangles "▲"
colored in gray in (c) to (f) indicate the acoustic centers calculated from the model. The colour scale indicates the non-dimensional
415   **acoustic intensity.**

In order to quantitatively evaluate the accuracy of localization based on vibration signals generated by particle impacts, we

conducted computations of acoustic images for 10 impact locations. The coordinate of the impact location was determined by

considering the center of the reconstructed sound source image through model inversion. Furthermore, the localization error

was determined by measuring the width of the main lobe at 70% of the peak intensity of the sound source. Finally, the

420   normalized coordinates $r_j^{m,t}$ were calculated by dividing the data obtained from the model inversion by the real coordinates.

As a result, the dimensionless localization accuracy in both X and Z directions on the plane was obtained, as shown in Fig. 12.

The results reveal that the data for each impact location are very close to the value of one, suggesting a good agreement between

the locations obtained by model-based inversion and the true coordinates. In addition, the variation in $r_j^{m,t}$ values gradually

increases as the impact location moves away from the center of the PMA plate and approaches its edge.
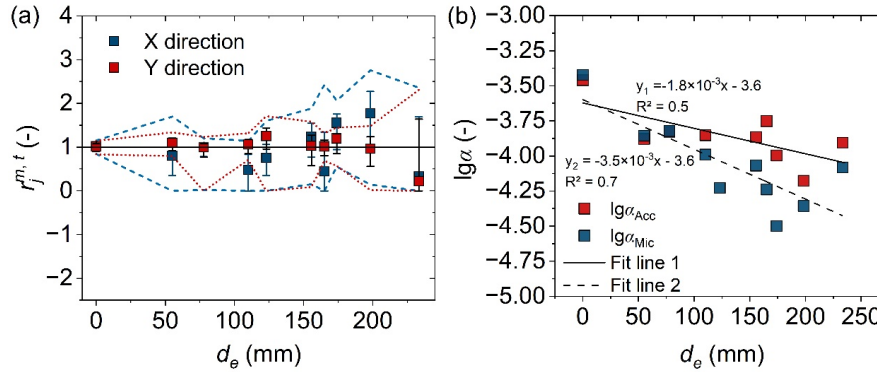
425

Figure 12: The ratio $r_j^{m,t}$ of the coordinates of a particle impact location and lgα as functions of the eccentricity distance d_e. (a)
The ratio was calculated based on acoustic images by the model inversion to the true coordinates of the sphere impact location for
particle size class j = 4. The boxes in green and red are the results for the X and Z directions, respectively. The dashed / dotted lines
and the error bars indicate the beam pattern resolution that covers a range of 30% and 10% below the peak value, respectively. (b)
430 **The values of lgα calculated from the data presented in Tab. 3, and by fixing the exponent β of the power law relation between A_{max}**
and D.

4 Discussion

4.1 Effect of bedload impact location on the PMA signal response

4.1.1 Maximum amplitude

435   The maximum amplitude of a packet $A_{Max,P}$ for the acceleration and the microphone signal shows similar trends with

increasing particle size for power-law approximations of the data (Fig. 8), except for the largest size class (D = 116.4 mm).

The results indicate an asymptotic behaviour of reaching an upper (maximum) limit of $A_{Max,P}$ for larger particles, which

shows similarities with the results obtained by finite element modelling for the SPG system in *Chen et al.* (2022a) and observed

for the Obernach flume experiments data for the saltation particles in *Chen et al.* (2022b). This resembles the asymptotic

440   behaviour of the signal frequency reaching a lower limit for larger particles (*Rickenmann*, 2017). The following two reasons

may be raised to explain this behaviour: i) The low impact velocity caused by small accelerating distance for the large particles

measured from the sphere center to the plate which is 10 cm for all size classes. ii) The maximum particle size that can be

detected by an impact plate system may be essentially determined by the total mass of the plate, which is indicated by theory

(Thorne, 2014) and by Erlenbach data for the SPG system (*Rickenmann*, 2017).

445   We should note the fact that the PMA system measures acceleration vibrations using an accelerometer, while the SPG system

measures deformation velocity using a geophone, when comparing the two systems. Furthermore, the PMA and SPG plates

are quadratic and rectangular, respectively, with a thickness of 15 mm and comparable boundary constraints. In terms of

structural dynamics, the material deformation velocity of the SPG plate may be smaller than that of the PMA plate under an

impact, but it is not comparable to that of the internal plate of the PMA system. One may rigorously compare the differences

450   in signal types recorded by different types of sensors. Thus, we integrated the acceleration signals from the PMA system to

obtain material deformation velocity signals (Fig. 8b), and observed that the maximum amplitude of the velocity signals

recorded by the geophone in the SPG system is approximately equal to that of the PMA velocity signals.

For the PMA system, the amplitude of the acceleration signal packet generated by eccentric impacts exhibits an attenuation

ranging from approximately 19% to 38% compared to centric impacts across all particle size classes, as illustrated in Fig. 8a.

455   As a result, the presence of eccentric impacts can lead to an underestimation of bedload particle size when using a calibration

relationship between the signal amplitude and particle size. This observation is qualitatively consistent with findings obtained

with the SPG system (*Chen et al.*, 2022a). However, compared to the impact test results obtained for the SPG system in *Chen

et al.* (2022a), the decay in signal amplitude $A_{Max,P}$ for the PMA system is relatively smaller when the impact location is

moved from the center to an eccentric position. This indicates that the acceleration signal from the PMA system is

460   comparatively less sensitive to changes in particle impact location than the SPG system. This discrepancy is likely due to the

different sensor mounting positions in the two systems. In the PMA system, the acceleration sensor is mounted on the internal

plate, whereas the geophone in the SPG system is positioned on the underside of the plate. As a result, the dissimilarities in

elastic wave propagation distance and refraction at the component interface contribute to the different sensitivities of the signal

responses to impacts in these two systems.

465   In contrast, the amplitude of the signal packet from the microphone, when excited by an eccentric impact, exhibited a decrease

ranging from 13% to 60% compared to the centric impact (see Fig. 8c). The attenuation in microphone signal amplitude

surpasses the reduction observed in the acceleration signals, indicating that the microphone signals are more sensitive to the

changes in the impact location than the latter. By utilizing the signals captured by the microphone element arrays, we can

derive the location of the acoustic source on the PMA plate. This information can be then employed to eliminate the

470   acceleration variations due to changing impact locations by constructing an appropriate compensation function.

4.1.2 Impulses-mass coefficient

The impulses-mass coefficient k_{IPM} provides an effective way for the conversion of the vibration signals recorded by the PMA

system into the bedload mass transported over the plate. The values of k_{IPM} tend to change less with decreasing size for the

smallest several particle size classes for a constant impact location (Fig. 9), which indicates a qualitative agreement with the

475   results obtain by the SPG system (*Chen et al.*, 2022a). However, the variability of k_{IPM} calculated from the signals generated

by different impact locations increases with decreasing particle size. This is possibly because the smaller particles generate

less impulses due to the lower impact energy but at a higher frequency, which makes the generated elastic waves more sensitive to changes in the propagation medium in the PMA system due to changes of the impact locations. The decrease in the impulse coefficient k_{IMP} resulting from the PMA signals is generally consistent with findings from *Wyss et al.* (2016a)' flume experiments and the Erlenbach filed site (*Wyss et al.*, 2016b) utilizing the SPG system. However, direct comparison using deformation velocity signals show that the k_{IMP} values calculated using a threshold value of 0.1 V in our work are approximately 1.0 to 6.1 times of those reported by *Wyss et al.* (2016a and 2016c), except for the two smallest particle size classes. This is due to the fact that, as mentioned above, the installation positions of the accelerometer and the geophone sensor in the PMA and SPG systems are different, resulting in a larger number of signal impulses of the PMA system than of the SPG system. This may be also partly due to the PMA accelerometer output range being limited to 100 g, whereas the limiting 10 V for the SPG geophone sensor corresponds approximately to 500 g.

4.1.3 Centroid frequency

The centroid frequency f_{Cen} of the generated signals decreases with increasing particle size, demonstrating qualitative agreement with the findings of the SPG system (*Wyss et al.*, 2016a) and conclusions derived from the contact theory (*Thorne*, 2014). Specifically, the centroid frequency $f_{Cen-Vel}$ derived from the integrated PMA velocity in this study are somewhat lower than the predictions of the contact theory and slightly lower (ca. 0.5-0.8 times) than the results of the flume experiments conducted by *Wyss et al.* (2016a). This may be due to the fact that, as discussed by *Chen et al.* (2022a) in relation to the SPG system, the calculation of the centroid frequency is based on the signals within the entire packet generated by an impact event. In contrast, the contact theory considers the transient duration of the contact, which typically lasts only a few milliseconds, whereas the former usually persists for tens or hundreds of milliseconds. The discrepancy between the drop test results in this study and Wyss's flume experiment results may also be attributed to structural differences between the two systems. Furthermore, the process of integrating from the acceleration signal to the deformation velocity signal may also result in the loss of frequency.

Furthermore, the signal data reveal that the centroid frequency $f_{Cen-Mic}$ calculated from the microphone signals is a bit higher than that determined from the acceleration signals $f_{Cen-Acc}$. This indicates that the microphone sensor is slightly more sensitive to air fluctuations than the accelerometer responds to material vibrations of the internal plate of the PMA system, which is likely to be a result of different sensor types. Both sets of data indicate that the outcomes resulting from eccentric impacts tend to have larger f_{Cen} values than those resulting from centric impacts. This is likely to be due to the fact that the edge of the PMA structure is more complex and more constrained, resulting in higher frequency responses.

4.2 Improved estimation of particle size

We used signals generated at 10 different impact locations (see positions marked in red in Fig. 2b) for calibration, as presented in Tab. 3. The data in Tab. 3 indicates that the effect of impact location on the power-law coefficient α is much greater than that on β. In the following analysis, we can reasonably assume constant β values using the mean values as 2.26 and 2.22 for acceleration and microphone data, respectively. This is characterized by changes in the vertical axis intercept ($\lg\alpha$) of the

510 calibration relationship between signal amplitude and particle size in log-log coordinates as: $lg(A_{Max,P}) = lg(\alpha D^{\beta}) = lg\alpha + \beta lgD$. A similar shift in the calibration relationships was also observed in field and experimental measurements of bedload at different flow velocities utilizing the SPG system (*Wyss et al.*, 2016a).

For the remaining six impact locations (2.4, 3.4, 3.3, 4.4, 4.3, and 4.2, marked in blue in Fig. 2b), the data generated were then used for particle size validation, which was processed as follows: i) The calibrated data revealed a correlation between the

515 coefficient $\lg\alpha$ and the eccentricity distance d_e, as illustrated in Fig. 12b. ii) For particle sizes ranging from 19.9 mm to 116.4 mm, the signal data generated by particle impacts was used to calculate the sources' center coordinates using the acoustic model developed earlier in this study. iii) The value of d_e for each impact is to the distance from the acoustic center according to the model inversion to the center of the PMA plate. The value of α can be then calculated using the relationship $lg\alpha - d_e$. iv) With the previously determined value of α and the assumed constant value of β, along with the application of the power-

520 law relationship $A_{Max,P} = \alpha D^{\beta}$, the particle size D_E, after mitigating the influence of eccentricity, can be calculated as follows: $D_E = \frac{1}{\alpha_A}\overline{A_{Max,P}}^{\frac{1}{\beta}}$, where D_E and α_E are the optimized particle size and coefficient α after reducing the influence of eccentricity, respectively; $\overline{A_{Max,P}}$ is the mean value of the maximum amplitude of a packet for 10 repetitive impact tests.

For a better comparison between the optimized and the non-optimized predicted particle sizes, the packet amplitudes resulting from eccentric impacts (e.g., impact at 2.4, 3.4, ..., 4.2) were employed for the computation of particle size D_A. This was

525 achieved using variable calibration relationships, employing the original values of α, which were determined at different impact locations (1.4, 2.3, 3.2, and 4.1).
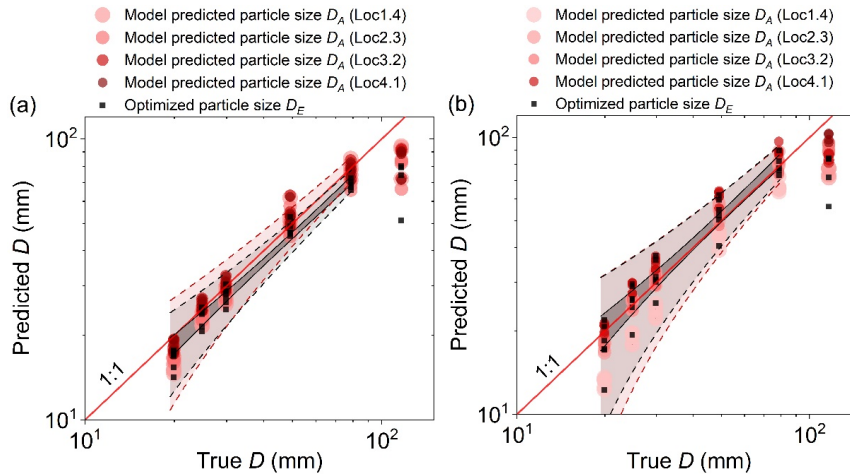
Figure 13: Predicted and optimized particle size vs. true particle size in the drop experiments with different impact locations. Particle sizes are derived from the signal amplitude recorded by the (a) accelerometer and (b) microphone sensor M05. The transparent red and black areas between the dashed lines represent the prediction bands for D_A and D_E, respectively. The black area between the solid lines is the confidence band for D_E.

Figure 13 compares the true size with the non-optimized particle size D_A and the optimized size D_E, derived from acceleration signals as well as microphone (sensor M05) signals, respectively. The results show that using the present acoustic model with the optimized coefficient α significantly reduces the variations in predicting bedload size by approximately 37% (up to 65%) on average over the entire particle size range, except for the largest size class. This is due to the fact that the signal amplitudes for the largest size class have not yet been used for calibration. The reason for this is that the impact velocity of the largest particle is observed to be significantly smaller than the rest of the particle classes, as the drop height remains at 10 cm for all size classes, which consequently causes some deviations in the signal amplitude. The microphone signals recorded by the PMA system are more sensitive to the impact location of the particles on the plate than the acceleration signals, as seen in Fig. 13. This could also explain why the optimized particle size using the microphone signals (Fig. 13b) performs better than that utilizing the acceleration signals (Fig. 13a). As a result, we may think that the acoustic model proposed in the present paper might be more effective for the improving the predicted particle size when employing signals captured by an accelerometer (or a geophone) mounted underside of an impact plate (of the impact plate system) rather than an internal plate. Nevertheless, the judicious utilization of multiple types of signals (both microphone and acceleration vibrations in this study) helps to improve the accuracy of particle size prediction compared to relying on only one-type signal features, thereby reducing spatial uncertainty.

4.3 Spatial resolution of the PMA system

Figure 11 illustrates acoustic images obtained through model inversion using the measured microphone signals generated by

particle impacts at different locations on the PMA plate. The acoustic pressure intensity shown in the images is normalized to

550   the maximum amplitude at the center of the calculated sound source. When the drop position is moved from the center to

eccentric locations of the PMA plate, the beam pattern shows some asymmetry, with notable side lobes. This characteristic

arises from the increased gain of interfering signals as the sound source approaches the plate's boundaries from its center.

Furthermore, the inversion results derived from the measured signals within the entire packet are complicated compared to the

results calculated using only the signal of the first wave. This applies in particular to the enhanced side lobes and a shift in the

555   center of the acoustic source. One factor that may contribute to these differences is that the refraction and reflection of the

acoustic signals by the PMA plate and the internal structural layers throughout an entire impact event may add to the

complexity of the inversion process.

Figure 12 presents the results of size class 4 particle impacts ($D = 49$ mm) at 10 different locations on the PMA plate. The data

obtained from all impact locations exhibit values close to one, indicating a general agreement between the inverted positions

560   determined by the model and the true coordinates. In addition, the beamwidth increases as the impact location moves away

from the center of the plate. This can be attributed to the fact that some components of the PMA system, such as the surrounding

locking components, might generate noise interference which could influence the structural dynamic responses and the

inversion results.

We also conducted numerical simulations for the case of a multipole with two sources, as shown in Fig. 7. The results

565   demonstrate that as the spacing between the sources decreases, the two main lobes merge, eventually reducing to a single lobe.

Under these conditions, the spatial resolution for detecting the multipole sources is approximately 0.12 m, as the two sources

become indistinguishable. However, it is important to note that this resolution is also dependent on particle size, with the

frequency value of 1600 Hz utilized in our numerical tests corresponding to a particle size of approximately 50 mm. By

employing higher frequency signals in simulations, the spatial resolution can be improved.

570   **4.4 Microphone array performance**

We evaluated the performance of the microphone element array and specifically investigated the effect of the number of

elements and their arrangement on the accuracy of the model inversion, as shown in Figs 5 and 6, respectively. The results

demonstrate that as the number of microphones increases, the accuracy improves (a decrease in the value of R_s). However,

the decrease of R_s tends to weaken with large numbers of microphone elements. Meanwhile the fourth arrangement Arr04

575   displayed the optimal performance of the four types of arrangements tested. These findings highlight the need of striking a

balance between accuracy and cost considerations, thus providing a reference for the design of monitoring systems. In the

future, it will also be worth investigating the inclusion of microphone elements into the existing surrogate bedload monitoring

system (*Rickenmann et al.*, 2022), and exploring the combined use of microphone and geophone signals, as we have tried with

the latest bedload monitoring device, the square pipe system (SPS). Such efforts have the potential to enhance the prediction

580   accuracy of bedload particle size and transport rates.

5 Conclusion

In this study, we have developed a novel acoustic bedload monitoring system, the phased microphone array (PMA) system, which consists of an accelerometer and an array of microphone elements. To evaluate the system's performance, we conducted controlled drop experiments using quartz particles with varying size, impact velocity, and impact location. Several essential

585   parameters that characterize the signal responses (acceleration and microphone signals) to an impact were investigated, including the maximum amplitude of a packet $A_{Max,Pac}$, the number of impulses per particle mass k_{IPM}, and the centroid frequency f_{Cen}. By analyzing the PMA signals generated by the particle impacts, we were able to determine the particle impact location on the plate. This allowed us to calculate the particle size using a pre-calibrated relationship, which effectively minimized variations associated with eccentric impacts, leading to improved accuracy of bedload size estimation. The main

590   conclusions of this study are as follows:

(1) In the drop experiments, the maximum amplitude of a signal packet measured by the accelerometer of the PMA system increases with increasing particle size for both centric and eccentric impacts. A similar trend is observed for the data recorded by the microphone sensor. For the PMA system, the amplitude of the acceleration and microphone signals generated by eccentric impacts can be attenuated by up to 38% and 60%, respectively, compared to centric impacts across the entire range

595   of size classes.

(2) The experimental data show that the number of signal impulses per particle mass k_{IMP} is dependent on particle size and impact location, with a nonlinear decreasing trend with increasing particle size. The centroid frequencies of the signals generated by both the accelerometer and microphone sensors generally decrease with increasing sphere size.

(3) We developed a theoretical model for acoustic imaging inversion based on bedload-generated signals. Using beamforming

600   techniques, we have successfully reconstructed acoustic images of bedload particle impacts, allowing their spatial location to be accurately determined. The accuracy of spatial localization is affected by factors such as particle size, the number of microphone elements, and their arrangement.

(4) The use of an established function between the power exponent and eccentricity distance significantly reduces prediction uncertainty in particle size caused by eccentric impacts by approximately 37% up to 65%. Optimal utilization of multiple types

605   of signals (both microphone and acceleration signals in this study) improves the accuracy of bedload size prediction. This offers potential advantages over the traditional independent use of either microphone systems or accelerometer/geophone plate systems.

Appendix A

Figure A1 shows different microphone arrangements with various element number ranging from 0 to 25 on the internal plate

610   of the PMA system. Figures A1a-A1d and A1i-A1k Different numbers of microphone elements which are used in numerical

simulation as presented in Fig. 5. Figures A1e- A1h Four arrangements Arr01 to Arr04 of the microphone elements arrays

with nine elements are used in the corresponding calculations of Fig. 6.
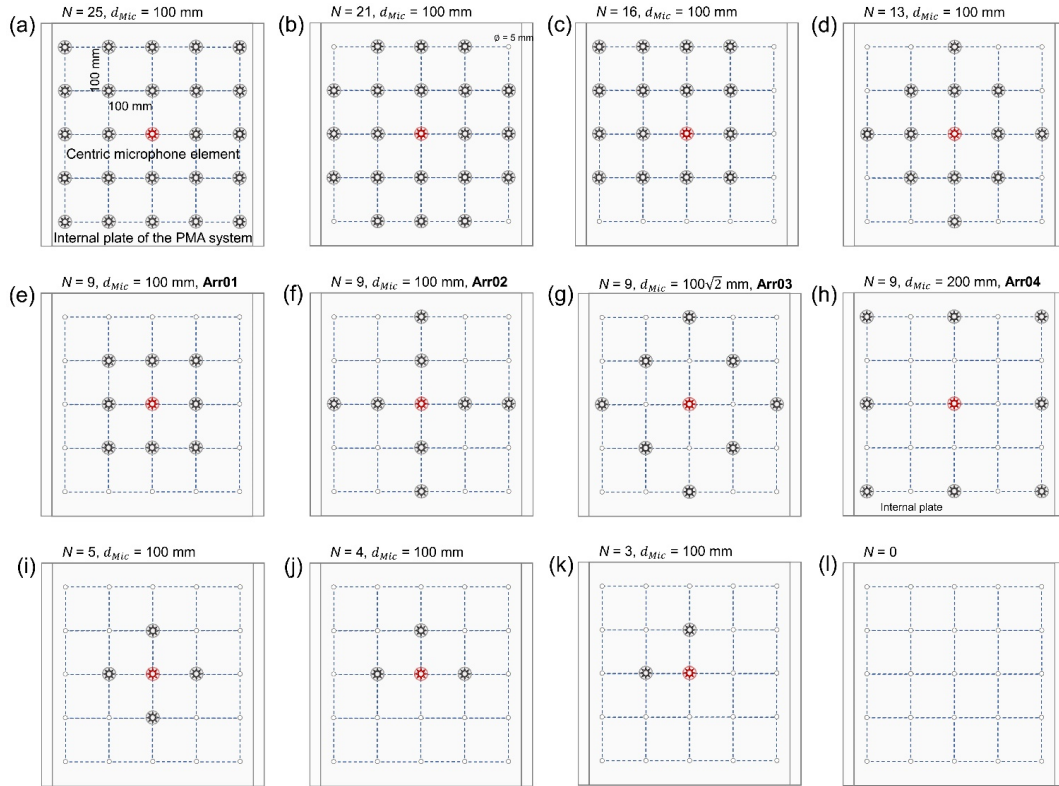
Figure A1: Microphone element arrangements with various number ranging from 0 to 25 positioned on the internal plate of the

615   **PMA system.**

Notations

$A_{FFT,m}$	amplitude obtained by FFT of the signal (V·Hz^{-1})
$A_{Max,P}$	maximum positive amplitude of a packet (V)
$A_{Pac,j}$	mean amplitude of a signal packet for each class j (V)
A_s	complex amplitude of the sound source (-)
C	cross-power matrix (-)

c	sound speed (m s^{-1})
D	particle size (m)
d_e	eccentricity distance (m)
D_j	mean particle size for class j (mm)
d_{Mic}	spacing distance of the microphone elements (m)
D_{pg}	difference between the measured or recorded pressure (Pa^2)
f	frequency of interest (Hz)
f_{Cen}	centric frequency (Hz)
FFT	fast Fourier transform (-)
f_S	sampling frequency (Hz)
g	steering vector (-)
$I_{i,j}$	signal impulses triggered by one impact of a single particle for experimental run i and particle size class j (-)
k	wave number (m^{-1})
k_{IPM}	number of impulses per particle mass (kg^{-1})
L_P	length of a signal packet (s)
L_{PMA}	length of the PMA plate (m)
M	particle mass (kg)
$M_{i,j}$	particle mass for experimental run i and particle size class j (kg)
N	number of microphone elements (-)
p	N-dimensional vector of pressure data (-)
p*	complex conjugate transpose of **p** (-)
P_{Norm}	non-dimensional acoustic intensity (-)
$r_j^{m,t}$	ratio of coordinates obtained from model inversion to the real (-)
R_S	resolution of the microphone array (m)
SNR	signal-noise ratio (-)
T	block length (s)
V_A	impact velocity in the air (m s^{-1})
V_W	impact velocity in the water (m s^{-1})
w	weighted steering vector (-)

w	angular frequency (Hz)
W_{PMA}	width of the PMA plate (m)
x_m	coordinate of microphone sensor m (-)
α	coefficient in power-law function (-)
β	coefficient in power-law function (-)
$\Delta t_{j,m}$	emission time delay (s)
Δx	grid size in the X direction (m)
Δy	grid size in the Y direction (m)
$\xi_{i,j}$	coordinate of a node on the scanning plane (-)
ρ_s	particle density (kg m^{-3})

Data availability statement

All data in this study were obtained through experiments and have been fully illustrated in figures and tables. No public datasets were used.

620 **Author contribution**

Zheng Chen: Conceptualization, Formal analysis, Investigation, Methodology, Software, Visualization, Funding acquisition, Writing – original draft preparation, Writing – review & editing; **Siming He:** Resources, Supervision, Writing – review & editing; **Alexandre Badoux:** Supervision, Writing – review & editing; **Dieter Rickenmann:** Supervision, Writing – review & editing.

625 **Competing of interest**

The authors declare that there are no conflicts of interest to disclose.

Funding information

This study was supported by the National Natural Science Foundation of China NSFC (grant 42307254 awarded to ZC), the 2022 Open Fund Research at the State Key Laboratory of Hydraulic and Mountain River Engineering (grant SKHL2224 awarded to ZC), and the State Key Laboratory of Geohazard Prevention and Geoenvironment Protection Independent Research

Project (grant SKLGP2022Z024 awarded to ZC).

Acknowledgements

The first author thanks Huijuan Chen, Jing Xu, and his colleagues of Chengdu University of Technology for their support with the additional laboratory experiments.

635 **References**

Antoniazza, G., Dietze, M., Mancini, D., Turowski, J. M., Rickenmann, D., Nicollier, T., Boss, S. and Lane, S. N.: Anatomy of an Alpine Bedload Transport Event: A Watershed-Scale Seismic-Network Perspective, J. Geophys. Res. Earth Surface, 128, e2022JF007000, doi:10.1029/2022JF007000, 2023.

Bakker, M., Gimbert, F., Geay, T., Misset, C., Zanker, S. and Recking, A.: Field application and validation of a seismic bedload
640 transport model, J. Geophys. Res. Earth Surface, 125, e2019JF005416, doi: 10.1029/2019JF005416, 2020.

Barton, J. S., Slingerland, R. L., Pittman, S., and Gabrielson, T. B.: Monitoring coarse bedload transport with passive acoustic instrumentation: A field study, US Geol. Surv. Sci. Investig., Rep., 5091, 38-51, 2010.

Burtin, A., Cattin, R., Bollinger, L., Vergne, J., Steer, P., Robert, A., Findling, N., and Tiberi, C.: Towards the hydrologic and bed load monitoring from high–frequency seismic noise in a braided river: The "torrent de St Pierre", French Alps, J. Hydrol.,
645 408, 43–53, doi:10.1016/j.jhydrol.2011.07.014, 2011.

Camenen, B., Jaballah, M., Geay, T., Belleudy, P., Laronne, J. B., and Laskowski, J. P.: Tentative measurements of bedload transport in an energetic alpine gravel bed river, In River flow, September 2012, 379–386, https://hal.inrae.fr/hal–02597879, 2012.

Cassel, M., Lavé, J., Recking, A., Malavoi, J. R., and Piégay, H.: Bedload transport in rivers, size matters but so does shape,
650 Sci. Rep., 11, 508, doi:10.1038/s41598-020-79930-7, 2021.

Chen, Z., He, S., Nicollier, T., Ammann, L., Badoux, A. and Rickenmann, D.: Finite element modelling of the Swiss plate geophone bedload monitoring system, J. Hydraul. Res., 60, 792-810, doi:10.1080/00221686.2022.2059585, 2022a.

Chen, Z., He, S., Nicollier, T., Ammann, L., Badoux, A. and Rickenmann, D.: Signal response of the Swiss plate geophone monitoring system impacted by bedload particles with different transport modes, Earth Surf. Dyn., 10, 279-300, doi:
655 10.5194/esurf-10-279-2022, 2022b.

Geay, T., Belleudy, P., Gervaise, C., Habersack, H., Aigner, J., Kreisler, A., Seiz, H., and Laronne, J. B.: Passive acoustic monitoring of bed load discharge in a large gravel bed river, J. Geophys. Res. Earth Surface, 122, 528–545,

doi:10.1002/2016JF004112, 2017.

Gimbert, F., Fuller, B. M., Lamb, M. P., Tsai, V. C., and Johnson, J. P.: Particle transport mechanics and induced seismic noise

660   in steep flume experiments with accelerometer - embedded tracers, Earth. Surf. Process. Landf., 44, 219–241, doi:10.1002/esp.4495, 2019.

Govi, M., Maraga, F., and Moia, F.: Seismic detectors for continuous bed load monitoring in a gravel stream, Hydrol. Sci. J., 38, 123–132, doi:10.1080/02626669309492650, 1993.

Habersack, H. M., and Laronne, J. B.: Evaluation and improvement of bed load discharge formulas based on Helley–Smith

665   sampling in an alpine gravel bed river, J. Hydraul. Eng., 128, 484-499, doi:10.1061/(ASCE)0733-9429(2002)128:5(484), 2002.

Hsu, L., Finnegan, N. J., and Brodsky, E. E.: A seismic signature of river bedload transport during storm events, Geophys. Res. Lett., 38, 1-6, doi:10.1029/2011GL047759, 2011.

Johnson, K. L.: Contact mechanics, Cambridge University Press, Kingdom of England, 1985.

Krein, A., Klinck, H., Eiden, M., Symader, W., Bierl, R., Hoffmann, L., and Pfister, L.: Investigating the transport dynamics

670   and the properties of bedload material with a hydro-acoustic measuring system, Earth. Surf. Process. Landf., 33, 152-163, doi:10.1002/esp.1576, 2008.

Mizuyama, T., Oda, A., Laronne, J. B., Nonaka, M., and Matsuoka, M.: Laboratory tests of a Japanese pipe geophone for continuous acoustic monitoring of coarse bedload, US Geol. Surv. Sci. Investig., Rep., 5091, 319-335, 2010.

Nicollier, T., Rickenmann, D., and Hartlieb, A.: Field and flume measurements with the impact plate: Effect of bedload grain-

675   size distribution on signal response, Earth. Surf. Process. Landf., 46: 1504–1520, doi:10.1002/esp.5117, 2021.

Nicollier, T., Antoniazza, G., Ammann, L., Rickenmann, D., and Kirchner J. W.: Toward a general calibration of the Swiss plate geophone system for fractional bedload transport, Earth Surf. Dyn., 10, 929-951, doi: 10.5194/esurf-10-929-2022, 2022.

Piantini, M., Gimbert, F., Bakker, M., Recking, A. and Nanni, U.: Using a dense seismic array to study fluvial processes in a braided river reach under flood conditions, LHB, 108, 2053314, doi:10.1080/27678490.2022.2053314, 2022.

680   Recking, A.: A comparison between flume and field bed load transport data and consequences for surface-based bed load transport prediction, Water Resour. Res., 46, W03518, doi:10.1029/2009WR008007, 2010.

Rickenmann, D.: Bed–load transport measurements with geophones and other passive acoustic methods, J. Hydraul. Eng., 143, 03117004, doi:10.1061/(ASCE)HY.1943–7900.0001300, 2017.

Rickenmann, D.: Variability of bed load transport during six summers of continuous measurements in two Austrian mountain

685   streams (Fischbach and Ruetz), Water Resour. Res., 54, 107-131, doi:10.1002/2017WR021376, 2018.

Rickenmann, D.: Bedload transport fluctuations, flow conditions, and disequilibrium ratio at the Swiss Erlenbach stream: results from 27 years of high-resolution temporal measurements, Earth Surf. Dyn., 12, 11-34, doi:10.5194/egusphere-2023-

964, 2023.

Rickenmann, D., and McArdell, B. W.: Continuous measurement of sediment transport in the Erlenbach stream using

690 piezoelectric bedload impact sensors, Earth. Surf. Process. Landf., 32, 1362–1378, doi:10.1002/esp.1478, 2007.

Rickenmann, D., and Fritschi, B.: Bedload transport measurements with impact plate geophones in two Austrian mountain

streams (Fischbach and Ruetz): system calibration, grain size estimation, and environmental signal pick–up, Earth Surf. Dyn.,

5, 669–687, doi:10.5194/esurf–5–669–2017, 2017.

Rickenmann, D., Turowski, J. M., Fritschi, B., Wyss, C., Laronne, J., Barzilai, R., Reid, I., Kreisler, A., Aigner, J., Seitz, H.,

695 and Habersack, H.: Bedload transport measurements with impact plate geophones: comparison of sensor calibration in different

gravel-bed streams, Earth. Surf. Process. Landf., 39, 928–942, doi:10.1002/esp.3499, 2014.

Rickenman, D., Ammann, L., Nicollier, T., Boss, S., Fritschi, B., Antoniazza, G., Steeb, N., Chen, Z., Wyss, C. and Badoux,

A.: Comparison of calibration characteristics of different acoustic impact systems for measuring bedload transport in mountain

streams, Earth Surf. Dyn., 10, 1165-1183, doi: 10.5194/esurf-10-1165-2022, 2022.

700 Rigby, J. R., Wren, D. G., and Kuhnle, R. A.: Passive acoustic monitoring of bed load for fluvial applications, J. Hydraul. Eng.,

142, 02516003, doi:10.1061/(ASCE)HY.1943–7900.0001122, 2016.

Rindler, R., Schwarz, S., Liedermann, M., Shire-Peterlechner, D., Kreisler, A., Aigner, J., Tritthart, M. and Habersack, H.:

Effective transport width—A methodology to describe the spatial variability of bedload transport, Int. J. Sediment Res., 38,

294-301, doi:10.1016/j.ijsrc.2022.09.007, 2023.

705 Roth, D. L., Brodsky, E. E., Finnegan, N. J., Rickenmann, D., Turowski, J. M. and Badoux, A.: Bed load sediment transport

inferred from seismic signals near a river, J. Geophys. Res. Earth Surface, 121, 725-747, doi:10.1002/2015JF003782, 2016.

Sijtsma, P.: Phased array beamforming applied to wind tunnel and fly-over tests, National Aerospace Laboratory NLR, Rep.,

1-48, 2010.

Thorne, P.: An overview of underwater sound generated by interparticle collisions and its application to the measurements of

710 coarse sediment bedload transport, Earth Surf. Dyn., 2, 531-543, doi: 10.5194/esurf-2-531-2014, 2014.

Thorne, P. D.: Laboratory and marine measurements on the acoustic detection of sediment transport, J. Acoust. Soc., 80, 899-

910, doi:10.1121/1.393913, 1986.

Tsai, V. C., Minchew, B., Lamb, M. P., and Ampuero, J. P.: A physical model for seismic noise generation from sediment

transport in rivers, Geophys. Res. Lett., 39, L02404, doi:10.1029/2011GL050255, 2012.

715 Tsakiris, A. G., Papanicolaou, A. T. N., and Lauth, T. J.: Signature of bedload particle transport mode in the acoustic signal of

a geophone, J. Hydraul. Res., 52, 185–204, doi:10.1080/00221686.2013.876454, 2014.

Turowski, J.M., Wyss, C.R. and Beer, A.R.: Grain size effects on energy delivery to the streambed and links to bedrock erosion,

Geophys. Res. Lett., 42, 1775-1780, doi:10.1002/2015GL063159, 2015.

Turowski, J. M., Böckli, M., Rickenmann, D., and Beer, A. R.: Field measurements of the energy delivered to the channel bed

720   by moving bed load and links to bedrock erosion, J. Geophys. Res. Earth Surface, 118, 2438–2450, doi:10.1002/2013JF002765, 2013.

Vasile, G.: Vibration data processing for bedload monitoring in underwater environments, Remote Sens., 12, 2797, doi:10.3390/rs12172797, 2020.

Wyss, C. R., Rickenmann, D., Fritschi, B., Turowski, J. M., Weitbrecht, V., and Boes, R. M.: Laboratory flume experiments

725   with the Swiss plate geophone bed load monitoring system: 1. Impulse counts and particle size identification, Water Resour. Res., 52, 7744–7759, doi:10.1002/2015WR018555, 2016a.

Wyss, C. R., Rickenmann, D., Fritschi, B., Turowski, J. M., Weitbrecht, V., and Boes, R. M.: Measuring bed load transport rates by grain–size fraction using the Swiss plate geophone signal at the Erlenbach, J. Hydraul. Eng., 142, 04016003, doi:10.1061/(ASCE)HY.1943–7900.0001090, 2016b.

730 Wyss, C. R., Rickenmann, D., Fritschi, B., Turowski, J. M., Weitbrecht, V., Travaglini, E., Bardou, E., and Boes, R. M.: Laboratory flume experiments with the Swiss plate geophone bed load monitoring system: 2. Application to field sites with direct bed load samples, Water Resour. Res., 52, 7760–7778, doi:10.1002/2016WR019283, 2016c.